Direct Synthesis of van der Waals Solids

Yu-Chuan Lin,[†] Ning Lu,[‡] Nestor Perea-Lopez,[§] Jie Li,[⊥] Zhong Lin,[§] Xin Peng,[‡] Chia Hui Lee,[†] Ce Sun,[‡] Lazaro Calderin,[†] Paul N. Browning,[†] Michael S. Bresnehan,[†] Moon J. Kim,[‡] Theresa S. Mayer,[⊥] Mauricio Terrones,[§] and Joshua A. Robinson[†,*]

[†]Department of Materials Science and Engineering and Center for 2-Dimensional and Layered Materials, The Pennsylvania State University, University Park, Pennsylvania 16802, United States, [‡]Department of Materials Science and Engineering, The University of Texas at Dallas, Richardson, Texas 75080, United States, [§]Department of Physics and Center for 2-Dimensional and Layered Materials, The Pennsylvania State University, University Park, Pennsylvania 16802, United States, and [⊥]Department of Electrical Engineering, The Pennsylvania State University, State College, University Park, Pennsylvania 16802, United States

ABSTRACT The stacking of two-dimensional layered materials, such as semiconducting transition metal dichalcogenides (TMDs), insulating hexagonal boron nitride (hBN), and semimetallic graphene, has been theorized to produce tunable electronic and optoelectronic properties. Here we demonstrate the direct growth of MoS_2, WSe_2, and hBN on epitaxial graphene to form large-area van der Waals heterostructures. We reveal that the properties of the underlying graphene dictate properties of the heterostructures, where strain, wrinkling, and defects on the surface of graphene act as nucleation centers for lateral growth of the overlayer. Additionally, we show that the direct synthesis of TMDs on epitaxial graphene exhibits atomically sharp interfaces. Finally, we demonstrate that direct growth of MoS_2 on epitaxial graphene can lead to a 10^3 improvement in photoresponse compared to MoS_2 alone.

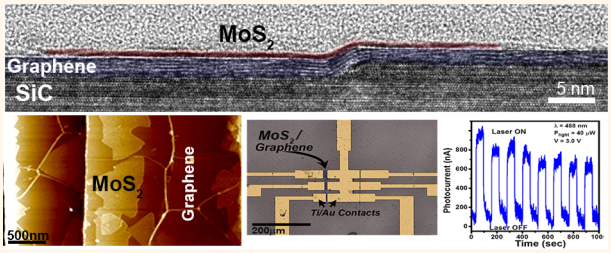

KEYWORDS: heterostructure · chemical vapor deposition · epitaxial graphene · transition metal dichalcogenides · layered materials · two-dimensional materials · photosensor · photocurrent · photoresponsivity

Graphene is considered the foundation of exciting new science in two-dimensional layered materials,[1] but it is only the "tip of the iceberg". Novel device designs necessarily require additional high-quality film as either the barrier or active layer. Recently, hexagonal boron nitride (hBN) has attracted attention as a gate dielectric or substrate material for integration with graphene-based electronics as a gate dielectric or substrate material because its sp^2-hybridized bonding and weak interlayer van der Waals bonds result in a pristine interface.[2] This also leads to a decreased density of absorbed impurities that act as Coulombic scattering centers when designing novel layered heterostructures.[3−5] Additionally, two-dimensional dichalcogenide-based materials are of significant interest for their finite band gaps ranging from 3.5 eV for GaS[6] to <1 eV for $MoTe_2$ and WTe_2.[7] More specifically, transition metal dichalcogenides (TMDs) such as molybdenum disulfide (MoS_2), tungsten disulfide (WS_2), and tungsten diselenide (WSe_2), have gained momentum in recent years due to their applications in a variety of electronic and optoelectronic applications.[3] This is also complemented by the possibility to tune the energy band gap of TMDs from 0.8 to 2.1 eV through heterogeneous integration, thus producing entirely novel electronic and optoelectronic materials not yet synthesized.[8] These unique properties make TMDs promising candidates for high-performance, low-cost energy materials for use in flexible electronics, photovoltaics,[9] and energy storage.[10,11] Development of electronically tunable van der Waals solids (vdW) must start with high-quality substrate materials. Graphene and graphite are excellent templates for the growth of bilayer AB-stacked graphene,[12] topological insulators,[13] and other 2D materials such as hBN and MoS_2.[14−18] To date, progress in the development of vdW heterostructures has led to a variety of new phenomena.[16,18] However, these vdW structures are primarily fabricated *via* mechanical exfoliation using polymer membranes and micromanipulators to stack the individual 2D crystals.[4] The process of mechanical exfoliation, while often useful for demonstration purposes, can lead to interface contamination.[19] These defects

* Address correspondence to jrobinson@psu.edu.

Received for review January 20, 2014 and accepted March 18, 2014.

Published online March 18, 2014
10.1021/nn5003858

and adsorbates buried at the interface of the 2D crystals undoubtedly diminish the quality and performance of devices.[19] Therefore, the development of a growth technique to assemble these systems during synthesis is required for large-area, high-quality vdW solids. Several groups have demonstrated direct growth of bilayer vdW solids (two dissimilar layers) as the building block for further heterointegration. Liu *et al.*[14] used a two-step *ex situ* process to grow chemical vapor deposition (CVD) graphene followed by synthesis of hBN on the CVD graphene. Similarly, Shi *et al.*[15] utilized CVD graphene as the growth template to grow MoS_2 by flowing $(NH_4)_2MoS_4$ precursor. While these are significant advances in the pursuit of vdW solids, the use of CVD graphene on Cu requires sophisticated methods of Cu etching and transferring to avoid pinholes, tears, or surface contamination in the heterogeneous structures. This may limit the applicability of heterostructures based on CVD graphene simply due to variation in electronic properties due to polymeric contamination, mechanical strains, and substrate/vdW solid interface imperfections. In this work, we utilize epitaxial graphene (EG) on 6H-SiC as the growth template for direct growth of MoS_2, WSe_2, and hBN. Quasi-free-standing epitaxial graphene (QFEG), hydrogen-treated EG,[20] is also utilized as a growing template and compared to EG to understand the impact of the EG buffer layer. Epitaxial graphene is utilized because it provides several technological advantages: (1) graphene is already on an insulating substrate, requiring no transfer processes; (2) the interface between graphene and SiC is pristine and tailorable;[20] (3) the surface is free of polymeric and other contaminants found in transferred CVD graphene;[21] and (4) epitaxial graphene is typically quite robust under standard device fabrication processes.[22] However, there are also challenges to utilization of epitaxial graphene (uniform thickness over large areas, steps in the SiC surface) that must also be considered. Here, we utilize atomic force microscopy (AFM), Raman spectroscopy, transmission electron microscopy (TEM), X-ray photoelectron spectroscopy (XPS), and photocurrent measurements to elucidate the impact of epitaxial graphene properties on the resulting MoS_2/EG, hBN/EG, and WSe_2/EG heterostructures.

RESULTS AND DISCUSSION

The utilization of epitaxial graphene provides a near perfect template for synthesis of vdW solids due to its lack of dangling bonds, chemical inertness, and ability to remain intact under high stress. Additionally, many of the 2D layered materials are isostructural, belonging to the symmetry group $P6_3/mmc$.[23] However, on the basis of the lattice parameters of graphene, hBN, MoS_2, and WSe_2 (2.461, 2.50, 3.16, and 3.28 Å, respectively),[23]

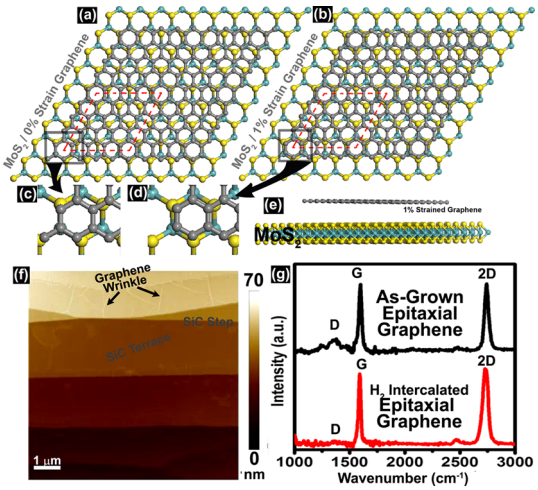

Figure 1. (a–e) DFT model of MoS_2/unstrained graphene and MoS_2/1% strained graphene predicts that residual strain in epitaxial graphene may enhance the structural symmetry in TMD/graphene heterostructures. (f) AFM image of as-grown epitaxial graphene demonstrating a smooth surface along with 5–10 nm steps in the SiC substrate. Wrinkles in graphene grown on SiC (0001) appear due to the CTE mismatch between graphene and SiC. (g) Raman spectra of as-grown epitaxial graphene and H_2-treated (hydrogenated) epitaxial graphene. Following hydrogenation, the D peak in EG is nearly eliminated by buffer layer passivation.

one may not expect epitaxial growth to proceed for transition metal dichalcogenides on graphene because a significant lattice mismatch exists. While this mismatch can be highly detrimental in 3D semiconductor epitaxy, there is a significant relaxation in the required lattice matching when growth proceeds *via* vdW interaction.[24] Density functional theory (DFT) clearly indicates poor commensurability between strain-free graphene and MoS_2 (Figure 1a,c), where the red dashed box is a guide for the eye, illustrating that the closest lattice match occurs at 3 and 4 unit cells (3–4) for MoS_2 and graphene, respectively. Figure 1c further illustrates the poor commensurability of the MoS_2/graphene (and other TMD/graphene combinations) heterostructures at the (3–4) matchup. However, the weak vdW interaction provides a route for "epitaxy" to occur in these structures. Ongoing DFT simulations, with van der Waals corrections as implemented in ONETEP,[25] have already shown homogeneous symmetrical reconstruction of the layered structures by inducing large strain on the layer of graphene at the local density approximation level of exchange and correlation functional.[26] Additionally, DFT indicates that the residual strain in epitaxial graphene (typical for graphene on SiC)[27] could impact epitaxy of the TMD by providing a route for improved commensurability (Figure 1b,d,e). Synthesis of high-quality epitaxial graphene was prepared by using an *in situ* hydrogen etch, followed by Si sublimation from the Si face of semi-insulating 6H-SiC (II–VI, Inc.) at 1700 °C, 100 Torr.[22] Some EG samples were further

exposed to molecular hydrogen (hydrogenation) at 1050 °C, 600 Torr, for 60 min to passivate the graphene/SiC (0001) buffer layer—referred as quasi-free-standing epitaxial graphene.[20] Hydrogenation typically results in the partial relaxation of residual strain in epitaxial graphene, which is evident in the red-shifted 2D Raman peak of the QFEG (Figure 1g). Raman and transmission electron microscopy confirm a uniform, continuous top layer of EG extending over the SiC ($1\bar{1}0n$) step edge and onto SiC (0001) terraces, with few-layer EG existing on the step edge after the growth (Supporting Information Figure S1).[22] The QFEG exhibits atomically smooth surfaces on the SiC terrace, as well as atomic-scale wrinkles that result from the coefficient of thermal expansion (CTE) mismatch that exists between EG and SiC (Figure 1f). This provides an ideal platform for understanding the interaction of heterolayers and the impact surface defects such as wrinkling, thickness, and surface potential variation have on the ability to form pristine vdW solids.[20] In addition to transforming the buffer into an additional graphene layer, Raman indicates that the quality of QFEG is significantly improved compared to EG, as the D peak is suppressed (Figure 1g). EG and QFEG are utilized as the base templates for direct integration with MoS_2.

The nucleation and growth of MoS_2 is strongly influenced by the characteristics of the underlying graphene. Heterolayers were synthesized *via* vapor-phase reaction of sublimed MoO_{3-x} and sulfur powders in a horizontal furnace, using both EG and QFEG as the growth template.[28] Using EG as the template, there is a distinct pattern for multilayer, pyramidal-shaped MoS_2 to form on the SiC (0001) terrace, while smooth mono- and bilayer MoS_2 forms at the SiC($1\bar{1}0n$) plane and extends outward (Figure 2a). On the other hand, under the same synthesis conditions, monolayer MoS_2 dominates the surface coverage on QFEG (Figure 2b) and is complemented by multilayered MoS_2 islands nucleating on wrinkles, SiC ($1\bar{1}0n$) step edge, and at graphene defects. The variation in nucleation and growth of MoS_2 on EG and QFEG is due to the difference in graphene strain, thickness,[29−31] and potentially buffer layer—all of which have significant impact on the chemical reactivity of graphene.[31] As-grown EG is thinner, exhibits 1% residual strain, and has a buffer layer that is partially covalently bound to the SiC substrate.[30] However, in the case of multilayer EG, where the impact of the buffer layer is expected to be significantly reduced due to increased EG thickness, MoS_2 tends to grow laterally rather than vertically. In the case of QFEG, the hydrogenation process passivates the buffer layer and decouples the graphene layers from the underlying SiC (Figure S2a). This results in some strain relief of the graphene (~0.3−0.5% residual strain), increases the layer thickness, and removes the EG buffer.

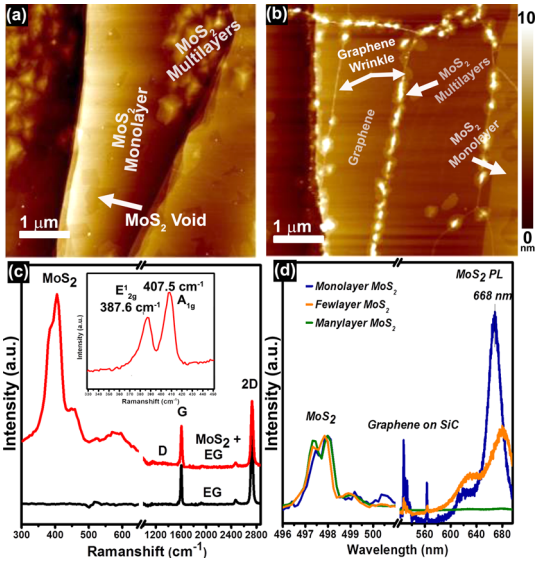

Figure 2. Atomic layers of MoS_2 grown on (a) EG and (b) QFEG demonstrating a clear difference in nucleation and growth for the two graphene template, which is attributed to the presence of enhanced residual strain and a buffer layer in EG compared to QFEG. In the case of QFEG, MoS_2 primarily nucleates on wrinkles and SiC step edges. (c) Raman spectra of MoS_2/EG and EG before the direct growth. Raman indicates that synthesis of MoS_2 does not induce additional defects in the EG or QFEG. Inset: E_{2g} and A_{1g} of the MoS_2 Raman features. (d) Photoluminescence from multilayer MoS_2 to monolayered MoS_2 after the growth, demonstrating that high-quality mono-, bi-, and multilayer MoS_2 is possible on epitaxial graphene.

This suggests that the chemical reactivity of EG is higher than QFEG due to strain and the presence of a buffer layer in EG, which results in a high density of TMD nucleation sites on EG.[20]

The MoS_2/EG(QFEG) heterogeneous structures exhibit high-quality structural, chemical, and interfacial properties (Figure 2c,d). Upon synthesis, the samples display MoS_2 peaks at 386 and 408 cm^{-1} ($E_{2g}{}^1$ and A_{1g} peaks, respectively)[32] and epitaxial graphene peaks at 1590 cm^{-1} (G peak) and 2740 cm^{-1} (2D peak)[30] in the Raman spectra (Figure 2c and inset). The intense $E_{2g}{}^1$ and A_{1g} vibration modes of the MoS_2 Raman spectra indicate that the MoS_2 is of high quality.[32] The $E_{2g}{}^1$ and A_{1g} peak spacing is also an indicator of layer thickness in TMDs[32,33] and is found to be 20.0 cm^{-1} for monolayer MoS_2 on epitaxial graphene. This value is 2 cm^{-1} larger than that in exfoliated monolayer MoS_2 and is due to the stiffening of the A_{1g} mode with *in situ* synthesis and CTE mismatch.[33] Photoluminescence (PL) from the MoS_2/EG(QFEG) heterostructures also provides evidence that the films are of high crystalline quality and can range from mono- to few-layer (Figure 2d) under current growth conditions.[34] Importantly, we note that Raman spectroscopy also confirms the direct synthesis of MoS_2 on EG and QFEG does not impact the quality of the underlying graphene (Figure 2c, no "D" peak). The element analysis on MoS_2/EG and MoS_2/QFEG *via*

XPS also confirms a proper stoichiometric ratio between Mo and S of 2, with no carbon bonding. The Mo 3d exhibits two peaks at 229.3 and 232.5 eV (Figure S2b), which is attributed to the doublet $3d_{5/2}$ and $3d_{3/2}$, respectively. The peaks corresponding to sulfur $2p_{1/2}$ and $2p_{3/2}$ orbitals in bonded sulfide are observed at 164 and 162.5 eV (Figure S2c). It should be noted that the resulting shapes of Mo and S in XPS are very similar, and thus only the MoS_2/QFEG heterostructure case is presented.

Following nucleation, there are distinct growth morphology differences between EG and QFEG. As noted in Figure 2a and Figure S3a, there exists a high density of MoS_2 islands on the terrace of EG, which are hypothesized to grow in a manner similar to that described by Stranski-Krastanov.[35] Here, the MoS_2 films form *via* a combination of layer-by-layer growth and 3D island growth, which is similar to synthesis of graphene on hBN.[36] The source of this islanding phenomenon may be related to the vertical propagation of a defect that initiates in the graphene layer (vacancy, strain-induced high chemical reactivity site, *etc.*; we later discuss the impact of graphene quality on MoS_2), which forms an additional nucleation site for adlayers to form and grow laterally outward from the central peak of the island (Figure 2b and Figure S3b). This phenomenon is also present in the QFEG case, although fewer isolated islands are identified on these samples where pristine QFEG exists. Rather, the QFEG wrinkles are more reactive due to the curved sp^2 π-bonds, which again induce localized strain and modification of the chemical reactivity of the graphene films.[37] The same phenomenon also occurs on QFEG step edges, similar to the synthesis of MoS_2 ribbons on highly oriented pyrolytic graphite (HOPG) surface.[38] The grain size of individual MoS_2 crystals on EG ranges from 200 to 1000 nm for the 10 min growth (Figure S4); however, these domains only partially cover the graphene surface. Longer growth times lead to a coalescence of MoS_2 domains into high-quality MoS_2 sheets. The MoS_2 domain size is increased by reducing the nucleation sites and prolonging the time for the growth. Surface potential force microscopy (SPFM) measurements provide evidence that the step edge region exhibits a 60 mV lower surface potential than that of graphene on the SiC terrace (Figure S5a,b), confirming that graphene on the SiC step edge is more reactive. The impact of MoS_2 synthesis on the quality of QFEG is correlated with the measured layer thickness of the MoS_2 overlayer. Evident in Figure 3, there are regions of high I_D/I_G ratios in the Raman spectra (Figure 3a,d), which closely match the presence of wrinkles in the graphene film, as well as areas of "thick" MoS_2 (Figure 3c,e). While wrinkles are present in as-grown QFEG (Figure 1f), the I_D/I_G is <0.05, indicating that high-quality QFEG exists prior to MoS_2 synthesis. It is not until after the synthesis of MoS_2 that significant degradation occurs at regions of the QFEG at wrinkle locations, which also correlates with broadening of the

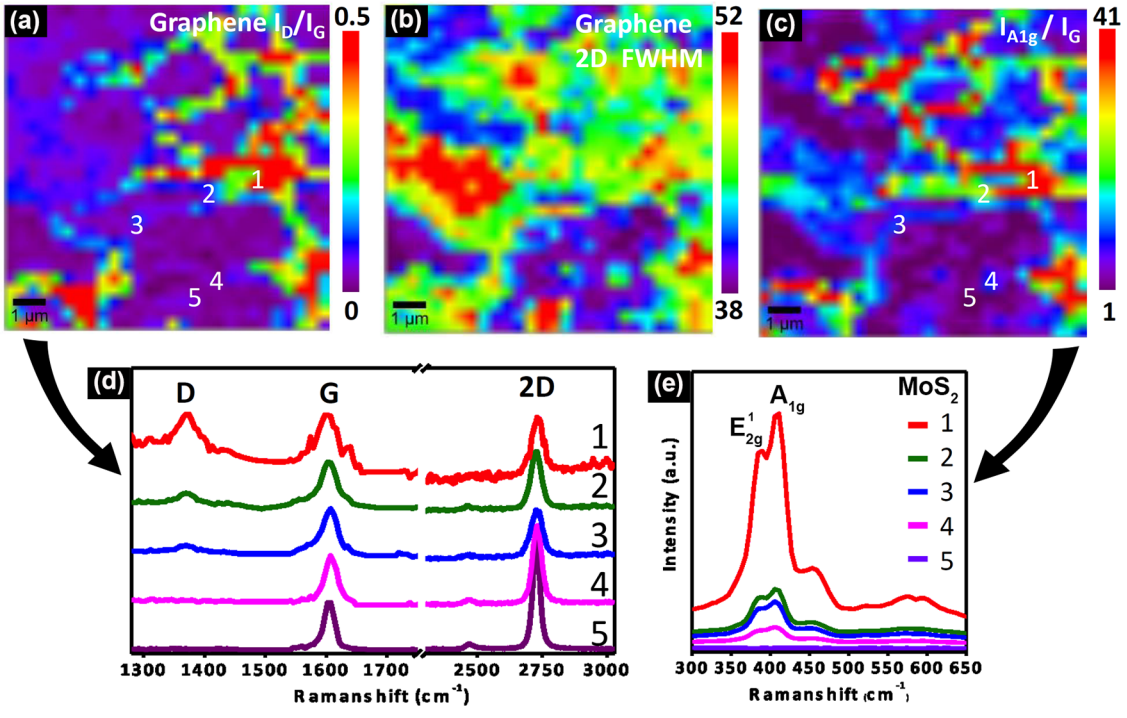

Figure 3. (a) Raman ratio map of QFEG I_D/I_G indicates that the synthesis of MoS_2 can induce defects in the underlying graphene layers at nucleation sites (*i.e.*, wrinkles, steps). (b) Corresponding 2D fwhm map of QFEG shows that broadening of the graphene 2D width can correlate the MoS_2 thickness. (c) Raman peak ratio map of $I_{A_{1g}}$ of MoS_2 to I_G of QFEG ratio indicates the MoS_2 distribution on QFEG, where higher ratios indicate "thicker" MoS_2. Comparing (a,c), there is a clear correlation between defects and MoS_2 thickness at QFEG wrinkles. (d,e) Raman spectra of numbered locations in the Raman map presented the MoS_2 and QFEG (a−c).

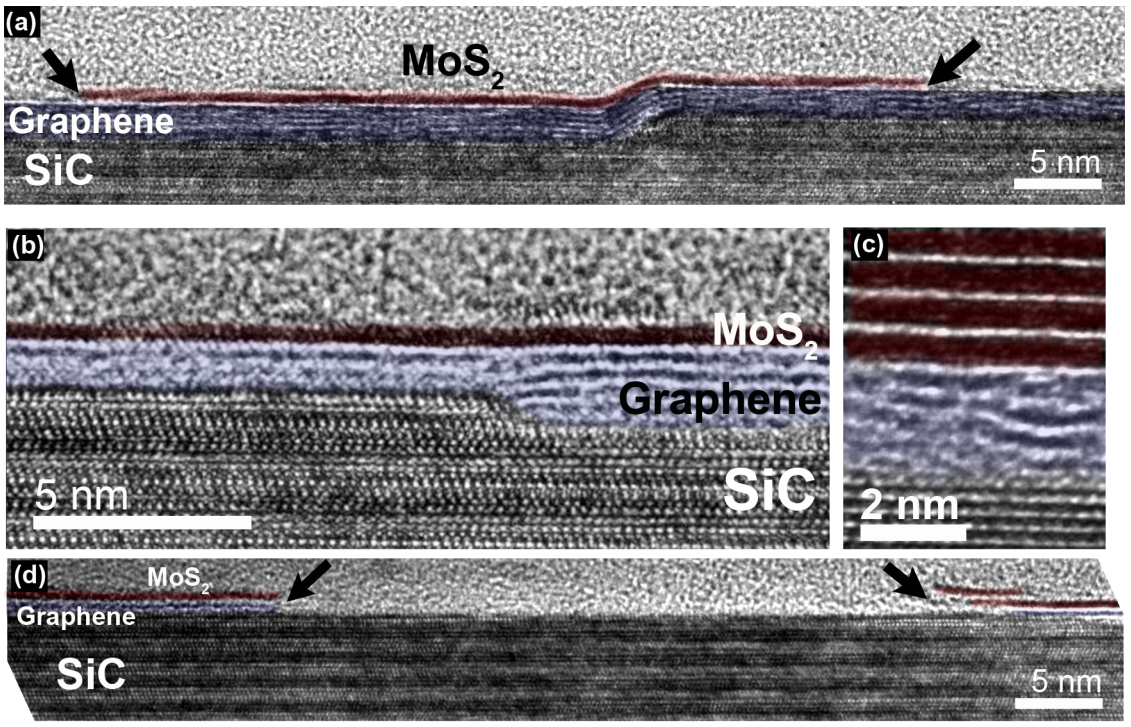

Figure 4. (a) Cross-sectional HRTEM of MoS_2/QFEG demonstrating the nucleation and subsequent lateral growth of MoS_2 on a SiC step edge covered with QFEG. In this case, the graphene thickness is consistent across the step, resulting in bending of the graphene and variation in strain of the EG layer. On the other hand, when the top graphene layer remains flat (b), the MoS_2 grows without regard of the changing morphology below. When the underlying graphene is defective (c), additional MoS_2 adlayers are present, which indicate that defects in the graphene can produce this MoS_2. Finally, MoS_2 nucleation and growth is promoted by the presence of graphene, while often it is found to be absent on bare SiC.

2D peak (Figure 3b). Correlating I_D/I_G (Figure 3a) with the ratio of the A_{1g} peak in MoS_2 and G peak in QFEG (Figure 3c) clearly indicates that the defect level is higher along QFEG wrinkles and in locations where the Raman spectra indicate bulk MoS_2 (Figure 3c,e). Interestingly, every MoS_2 island associated with a wrinkle appears to be bisected by the wrinkle (Figure 2b), suggesting that the nucleation of the MoS_2 occurs at the peak of the wrinkle and is followed by lateral growth of the layer. This scenario is highly plausible considering that the wrinkle apex is of highest stress—and thus the highest chemical reactivity.[31] It has been reported that chemical functionalization on graphene is energetically preferable to happen at the site with higher chemical reactivity due to a lower formation energy.[31] Thus, we speculate that the formation energy of MoS_2 nucleation is lower at the location with high chemical reactivity.

The direct synthesis of TMD on QFEG results in a pristine heterointerface. Transition electron microscopy cross-sectional micrographs confirm that monolayer MoS_2 nucleates on the $(1\bar{1}0n)$ step edges and subsequently extends onto the (0001) terrace in regions where the thickness of graphene does not vary over the $(1\bar{1}0n)/(0001)$ conjunction (Figure 4a). This suggests that the $(1\bar{1}0n)$ step edges may play a critical role in nucleation, which is consistent with the observation in AFM images of MoS_2/EG(QFEG) in Figure 2a,b. Furthermore, the MoS_2 layer appears to be "blind" to thickness variations in the underlying graphene when there are no defects in the top layer of the graphene (Figure 4b). Apparently, in the case where additional layers of graphene are formed in a manner as to maintain a flat surface profile, the graphene appears to shield the influence from the SiC morphology. On the other hand, when defective graphene is present at the surface of the graphene layer, there is almost always multilayered MoS_2 present (Figure 3c). Additionally, quite often it is found that MoS_2 nucleation and growth does not proceed on the SiC (0001) terrace when graphene is not present. Figure 4d demonstrates that the MoS_2 growth ends at the terminations of graphene, which suggests that graphene may serve as the catalytic layer for MoS_2 nucleation and growth. The similar case has been reported in the growth of MoS_2 on CVD graphene/Cu.[15] However, the MoS_2 grown directly on catalytic metals has not been reported.

Photoconductivity has been demonstrated on single-layer MoS_2, but the photoconductivity must be improved to be competitive to current state-of-the-art materials. Yin *et al.*[39] demonstrate a photoresponsivity of ~0.42 mA/W with at a photon intensity of 80 μW and drain bias of 1 V, while 7.5 mA/W is achieved at V_g = 50 V. This was improved upon by Zhang *et al.*[40] with the mechanically stacked heterostructures CVD MoS_2/CVD graphene, where the photoresponsivity

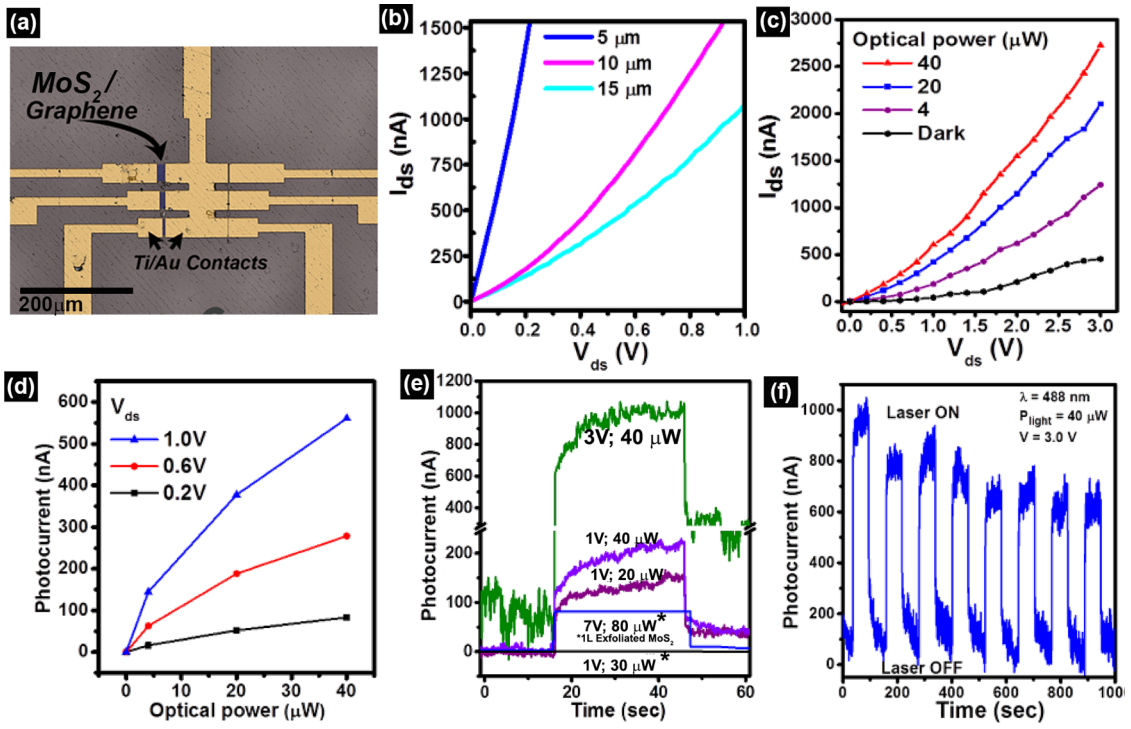

Figure 5. (a) Optical image of the fabricated MoS_2/graphene photosensor. (b) Room temperature electrical characteristic of a two-terminal MoS_2/QFEG photosensor shows the drain current (I_{ds}) *vs* voltage (V_{ds}) at different channel lengths (5, 10, and 15 μm). The output characteristics of the MoS_2/QFEG photosensor (c,d) when illuminated with 488 nm photon at increasing illuminating laser power and gate voltage. (e) Photoswitching behavior of the photosensor at different laser power (P_{light}) and V_{ds} compared to current literature.[39] (f) Transient measurement of the photosensor at V_{ds} = 3.0 V and P_{light} = 40 μW, demonstrating fast, stable response.

reached more than 10^7 A/W with the electrical gating effect. We also investigate photoconductivity and responsivity using two-terminal MoS_2/QFEG devices without back-gating fabricated *via* standard photolithography process to demonstrate the superiority of direct synthesis heterostructures.[41,42] The channel resistance is found to increase from hundreds of ohms to $\sim 10^6$ Ω as the channel length increases from 5 to 15 μm (Figure 5a). Interestingly, the drain current is similar to previous reports for MoS_2[39] and much lower than epitaxial graphene devices (Figure S7a),[22] indicating that the Ti/Au metal contacts have not contacted the underlying graphene, and that transport is dominated by MoS_2 in the channel. This is encouraging for the development of lateral TMD devices on graphene because the graphene has not shorted the device. This phenomenon is likely a result of the high interlayer resistance in vdW solids,[43] which provides a large potential barrier for vertical transport and results in charge being confined to the top MoS_2 layers when the ohmic metallization does not contact the underlying graphene. In the case where pinholes exist in the MoS_2 layer under the ohmic metallization, we find that current transport is dominated by graphene, and $I-V$ curves become highly linear with channel resistances <500 Ω. These devices were not considered for photocurrent measurements. Direct growth of MoS_2 on epitaxial graphene yields significant improvements in photoconductivity and responsivity. The MoS_2/QFEG photosensor device (Figure 5a) was investigated by exploring photocurrent under various optical powers and bias conditions. Ideally, the generation of photocurrent needs to match the basic condition that the incident photon energy must be greater than the optical energy gap (E_g) of MoS_2. Single-layer MoS_2 is reported to have a band gap of 1.83 eV corresponding to 676 nm in wavelength.[34] The MoS_2 from the direct growth in this study shows PL at 668 nm, corresponding to an optical energy gap 1.85 eV (Figure 2d). Under a constant excitation wavelength at 488 nm, and power ranging from 4 to 40 μW, the MoS_2/QFEG generates a power-dependent photocurrent ranging from 150 to 550 nA at V_{ds} = 1 V (Figure 5c,d). This represents a 200-fold increase in photocurrent compared to exfoliated MoS_2.[39] Photoresponsivity is a crucial parameter when evaluating the performance of a photosensor. It is defined as $R = I_{ph}/P_{light}$, where I_{ph} is photogenerated current and P_{light} is the total incident optical power on the photosensor.[39,40] In the current MoS_2/EG device with a 15 μm channel length, V_{ds} = 1 V, and V_g = 0 V, we find R = 40 mA/W when P_{light} = 40 μW. Previously, the reported R of similarly biased monolayer MoS_2 photosensor with P_{light} = 80 μW was 0.42 mA/W,[39] which was 2 times that of a WS_2 photosensor device (0.22 mA/W).[44] Additionally, using a 514 nm laser, the photoresponsivity is further increased to 79 mA/W

when P_{light} = 40 μW and V_{ds} = 1 V (Figure S6). Thus the MoS_2/EG photosensor represents a minimum 100-fold improvement in photoresponsivity and 1000-fold improvement in absolute photoconductivity, compared to exfoliated single-layer MoS_2 (Figure 5e). At V_{ds} = 1 V, the photocurrent increases from 150 to 230 nA when the P_{light} increases from 20 to 40 μW. The photocurrent further increases to 1000 nA when the V_{ds} increases from 1 to 3 V at constant P_{light} of 40 μW. Moreover, the stability of this switching behavior is further tested by sequentially turning the illumination laser on (30 s) and off (30 s). Figure 5f shows the photocurrent stability over 1000 s of continuous operation. Correlating material characterization with optoelectronic performance, the improvement can be ascribed to (1) the high crystal quality of MoS_2 grown on QFEG, and the presence of pristine surfaces and atomically sharp interfaces of the MoS_2/QFEG heterostructures; and (2) the underlying QFEG screen charge scattering sites that may be present on the SiC substrate. To deconvolute the source of the photoresponse, we also examine QFEG-only photosensors. These photosensors exhibit negligible response due to photon excitation (Figure S7b), confirming theoretical predictions that the primary photon interaction, and thus photocurrent generation, of MoS_2/QFEG is attributed to the additive MoS_2 layer on the graphene.[45]

To determine the universality of epitaxial graphene as a template for the synthesis of high-quality van der Waals solids, we further demonstrate the integration of tungsten diselenide (WSe_2) and hexagonal boron nitride on QFEG substrates. Cross-sectional HRTEMs of WSe_2/QFEG/SiC (Figure 6a) and hBN/QFEG/SiC (Figure 6b) and their corresponding Raman signatures (Figure 6c,d) indicate that the underlying graphene is not damaged by the synthesis process.[2] Additionally, TEM confirms a clean van der Waals gap between the different layered materials. After the growth of hBN on QFEG, several Raman peaks are present at 1368 cm^{-1}, which is suggested as the combination of the E_{2g} mode of B−N vibration at 1372 cm^{-1} and the D peak of graphene at 1360 cm^{-1}.[14] The very minor peak at 2950 cm^{-1} (corresponding to the graphene Raman D+G mode) indicates that the growth of hBN only nominally increases the defect density. Evident from XPS (Figure 6d−f), CVD-deposited hBN is nearly stoichiometric and does not affect the chemistry of graphene underneath. The high-resolution N1s and B1s core level peaks in Figure 6d,f are at 191.5 and 398.8 eV, respectively, consistent with reference values for bulk hBN.[47] Additionally, the C1s peak remains unchanged following hBN synthesis. In the WSe_2/QFEG case, the prominent Raman peaks of the E_{2g}/A_{1g} from WSe_2 and the G peak at 1597 cm^{-1} from graphene/SiC indicate the possibility to integrate other TMD layers over the epitaxial graphene without significantly impacting the graphene structure. As a result, the utilization of an epitaxial graphene template may be considered as an excellent candidate for development of a broad range of vertical heterostructures.

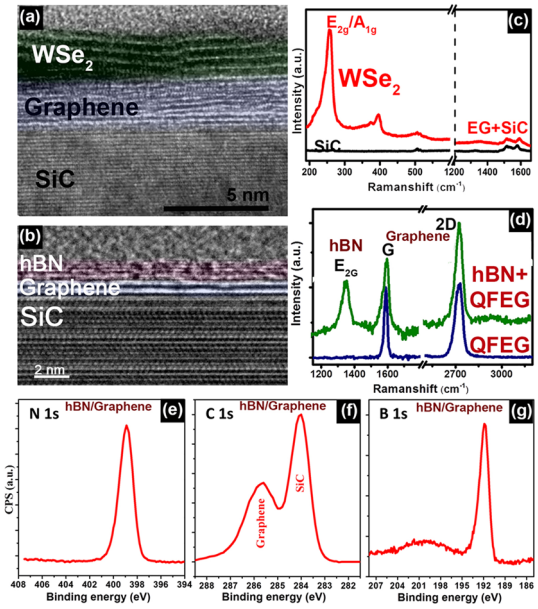

Figure 6. Transmission electron microscopy of (a) WSe_2/QFEG and (b) hBN/QFEG reveals that the interface within layers and between heterolayers is pristine, with no observable defects. Additionally, Raman spectra (c,d) of quasi-free-standing epitaxial graphene (QFEG), QFEG/hBN, and QFEG/WSe_2 indicate that high-quality van der Waals solids have been grown on QFEG. There is also a small photoluminescence background following hBN synthesis, which has been reported from the CVD-grown hBN thin film.[16] (e−g) High-resolution XPS spectra of B1s, C1s, and N1s core level peaks from hBN grown on QFEG. The peak positions of as-grown B1s and N1s peaks are similar to bulk hBN values, and peak shape indicates no significant contributions from carbon or oxygen bonding in the hBN. The energy loss at 200 eV in (g), which is higher than B1s by 9 eV, is attributed to the $\pi-\pi^*$ interaction in hexagonal phase BN crystals.[46]

CONCLUSIONS

In conclusion, high-quality epitaxial graphene has been synthesized and utilized as the growth template for vdW solids that include MoS_2, WSe_2, and hBN. TMDs are synthesized by gas-phase reaction of MoO_3 and WO_3 and S and Se, while hBN is synthesized on epitaxial graphene by utilizing ammonia borane as the precursor in a tube CVD chamber. This demonstrates that epitaxial graphene may be a universal substrate for a variety of deposition methods and materials. This is due to the presence of residual strain and wrinkles, which play an important role in the nucleation of vdW solids. It has been found that the QFEG template has less MoS_2 nucleated on the terrace than EG template due to the strain relief and elimination of the underlying buffer—both expected to increase chemical reactivity of the graphene. Photosensors based on direct growth MoS_2/QFEG heterostructures exhibit an improvement in photoresponsivity by a minimum of 200-fold, demonstrating the high quality in heterostructures from the direct growth. Finally, we have

provided strong evidence that epitaxial graphene can be an excellent candidate for building large-area vdW solids that will have extraordinary properties and performance. The two-terminal electrical measurements on synthesized layers here show that the interlayer resistances between the graphene and top heterolayers are high enough and that the stacks are not "shorted" simply by the presence of graphene, rather it will be proper contacting of the individual layers that will be critically important.

EXPERIMENTAL METHODS

Synthesis. Epitaxial graphene is grown on diced SiC wafers *via* sublimation of silicon from 6H-SiC (0001) at 1700 °C for 15 min under 1 Torr Ar background pressure. Quasi-free-standing graphene is prepared by exposing epitaxial graphene to 600 Torr H_2 at 1050 °C for 120 min to intercalate hydrogen at the graphene/SiC (0001) interface.[22] Growth of MoS_2 layers was accomplished using MoO_3 powders (0.1 g) placed in a ceramic crucible located in the center of a 2 in. tube furnace. Sulfur powders are placed in a second ceramic crucible up stream and held at 130 °C during the reaction. The epitaxial graphene/SiC for growing MoS_2 was put at the downstream side. The MoO_3 and S vapors were transported to the epitaxial graphene/SiC substrates by pure Ar flowing gas (Ar = 50 sccm, chamber pressure = 5 Torr). The heating zone was heated to 670 °C at a ramping rate of 15 °C/min.[28] Growth of WSe_2 layers on epitaxial graphene were accomplished by first thermally evaporating 5 nm WO_3 on QFEG/SiC. The WO_3/QFEG/SiC was subsequently exposed to selenium vapor by heating pure selenium metal to 500 °C upstream in the tube furnace. This process converts the WO_3 to WSe_2, as discussed elsewhere.[44] Growth of hBN layers on QFEG was accomplished in a 75 mm diameter horizontal tube furnace *via* thermal CVD method utilizing ammonia borane (NH_3BH_3) precursor. Solid ammonia borane powder is sublimed at 135 °C and transported into the tube furnace by H_2/Ar carrier gas (5% of total flow rate). Growth occurs at 1075 °C and 250 mTorr in 5 min. After the growth, the ammonia borane carrier gas is turned off and the furnace is allowed to cool to room temperature slowly in a 250 mTorr Ar/H_2 environment.[2]

Fabrication and Measurement of MoS_2 Photosensor Devices. Two-terminal photosensor devices were fabricated using standard ultraviolet photolithography. The sensors are with various source-drain spacing, which ranges from 1 to 15 μm. Titanium/gold (30/100 nm) ohmic contacts were deposited in a similar fashion to our graphene devices, which utilizes an oxygen plasma pretreatment.[41] Photocurrent measurements were carried out at room temperature in ambient conditions and were coupled to a Renishaw micro-Raman spectroscopy with a 488 nm laser. The electrical conduction data were collected with a power source and a Keithley 2400 meter.[44] The photocurrent measurements at low temperature were acquired using a Lakeshore cryogenic probe station.

Characterization. The as-grown heterostructures were characterized using Raman spectroscopy, AFM, XPS, and TEM. A WITec CRM200 confocal Raman microscope with a 488 nm laser wavelength was utilized for structural characterization. For as-grown epitaxial graphene, the SiC background signal was subtracted using a direct subtraction of the SiC substrate from the spectra.[30] A Bruker Dimension with a scan rate of 0.5 Hz was utilized for the AFM measurements. A Kratos Axis Ultra XPS system utilizing an Al Kα source with energy of 1486 eV was used for XPS analysis. The TEM cross-sectional samples were made by utilizing a NanoLab dual-beam FIB/SEM system. Protective layers of SiO_2 and Pt were deposited to protect the interesting region during focused ion beam milling. TEM imaging was performed using a JEOL 2100F operated at 200 kV.

Conflict of Interest: The authors declare no competing financial interest.

Acknowledgment. This work at the Penn State and UT Dallas was supported by the Center for Low Energy Systems Technology (LEAST), one of six centers supported by the STARnet phase of the Focus Center Research Program (FCRP), a Semiconductor Research Corporation program sponsored by MARCO and DARPA. Support for the WiteC Raman system, Bruker Dimension AFM, Kratos Axis Ultra XPS, and nanofabrication facilities was provided by the National Nanotechnology Infrastructure Network at Penn State. We thank S.H. Kim and E. Hsiao (PSU-Chem Eng.) for SPFM measurements.

Supporting Information Available: AFM, Raman map, SPFM of EG, XPS, and measured photocurrent results under a 514 nm laser of MoS_2/QFEG hybrids and bare QFEG. This material is available free of charge *via* the Internet at http://pubs.acs.org.

REFERENCES AND NOTES

1. Novoselov, K. S.; Geim, A. K.; Morozov, S. V.; Jiang, D.; Zhang, Y.; Dubonos, S. V.; Grigorieva, I. V.; Firsov, A. A. Electric Field Effect in Atomically Thin Carbon Films. *Science* **2004**, *306*, 666–669.
2. Bresnehan, M. S.; Hollander, M. J.; Wetherington, M.; LaBella, M.; Trumbull, K. A.; Cavalero, R.; Snyder, D. W.; Robinson, J. A. Integration of Hexagonal Boron Nitride with Quasi-Free-standing Epitaxial Graphene: Toward Wafer-Scale, High-Performance Devices. *ACS Nano* **2012**, *6*, 5234–5241.
3. Geim, A. K.; Grigorieva, I. V. van der Waals Heterostructures. *Nature* **2013**, *499*, 419–425.
4. Dean, C. R.; Young, A. F.; Meric, I.; Lee, C.; Wang, L.; Sorgenfrei, S.; Watanabe, K.; Taniguchi, T.; Kim, P.; Shepard, K. L. Hone, Boron Nitride Substrates for High-Quality Graphene Electronics. *Nat. Nanotechnol.* **2010**, *5*, 722–726.
5. Britnell, L.; Gorbachev, R. V.; Jalil, R.; Belle, B. D.; Schedin, F.; Mishchenko, A.; Georgiou, T.; Katnelson, M. I.; Eaves, L.; Morozov, S. V.; *et al.* Field-Effect Tunneling Transistor Based on Vertical Graphene Heterostructures. *Science* **2012**, *335*, 947–950.
6. Sanz, C.; Guillén, C.; Gutiérrez, M. T. Influence of the Synthesis Conditions on Gallium Sulfide Thin Films Prepared by Modulated Flux Deposition. *J. Phys. D: Appl. Phys.* **2009**, *42*, 085108.
7. Gong, C.; Zhang, H.; Wang, W.; Colombo, L.; Wallace, R. M.; Cho, K. Band Alignment of Two-Dimensional Transition Metal Dichalcogenides: Application in Tunnel Field Effect Transistors. *Appl. Phys. Lett.* **2013**, *103*, 053513.
8. Lee, H. S.; Min, S.-W.; Chang, Y.-G.; Park, M. K.; Nam, T.; Kim, H.; Kim, J. H.; Ryu, S.; Im, S. MoS_2 Nanosheet Phototransistors with Thickness-Modulated Optical Energy Gap. *Nano Lett.* **2012**, *12*, 3695–3700.
9. Pu, J.; Yomogida, Y.; Liu, K.-K.; Li, L.-J.; Iwasa, Y.; Takenobu, T. Highly Flexible MoS_2 Thin-Film Transistors with Ion Gel Dielectrics. *Nano Lett.* **2012**, *12*, 4013–4017.
10. Jariwala, D.; Sangwan, V. K.; Lauhon, L. J.; Marks, T. J.; Hersam, M. C. Emerging Device Applications for Semiconducting Two-Dimensional Transition Metal Dichalcogenides. *ACS Nano* **2014**, *8*, 1102–1120.
11. Wang, J.-Z.; Lu, L.; Lotya, M.; Coleman, J. N.; Chou, S.-L.; Liu, H.-K.; Minett, A. I.; Chen, J. Development of MoS_2–CNT Composite Thin Film from Layered MoS_2 for Lithium Batteries. *Adv. Energy Mater.* **2013**, *3*, 798–805.
12. Yan, K.; Peng, H.; Zhou, Y.; Liu, Z. Formation of Bilayer Bernal Graphene: Layer-by-layer Epitaxy via Chemical Vapor Deposition. *Nano Lett.* **2011**, *11*, 1106–1110.
13. Dang, W.; Peng, H.; Li, H.; Wang, P.; Liu, Z. Epitaxial Heterostructures of Ultrathin Topological Insulator Nanoplate and Graphene. *Nano Lett.* **2010**, *10*, 2870–2876.

14. Liu, Z.; Song, L.; Zhao, S.; Huang, J.; Ma, L.; Zhang, J.; Lou, J.; Ajayan, P. M. Direct Growth of Graphene/Hexagonal Boron Nitride Stacked Layers. *Nano Lett.* **2011**, *11*, 2032–2037.
15. Shi, Y.; Zho, W.; Lu, A.-Y.; Fang, W.; Lee, Y.-H.; Hsu, A. L.; Kim, S. M.; Yang, H. Y.; Li, L.-J.; Idrobo, J.-C.; *et al.* van der Waals Epitaxy of MoS_2 Layers Using Graphene as Growth Templates. *Nano Lett.* **2012**, *12*, 2784–2791.
16. Radisavljevic, B.; Radenovic, A.; Brivio, J.; Giacometti, V.; Kis, A. Single-Layer MoS_2 Transistors. *Nat. Nanotechnol.* **2011**, *6*, 147–150.
17. Kubota, Y.; Watanabe, K.; Tsuda, O.; Taniguchi, T. Deep Ultraviolet Light-Emitting Hexagonal Boron Nitride Synthesized at Atmospheric Pressure. *Science* **2007**, *317*, 932–934.
18. Gorbachev, R. V.; Geim, A. K.; Katsnelson, M. I.; Novoselov, K. S.; Tudorovskiy, T.; Grigorieva, I. V.; MacDonald, A. H.; Morozov, S. V.; Watanabe, K.; Taniguchi, T.; *et al.* Strong Coulomb Drag and Broken Symmetry in Double-Layer Graphene. *Nat. Phys.* **2012**, *8*, 896–901.
19. Haigh, S. J.; Gholinia, A.; Jalil, R.; Romani, S.; Britnell, L.; Elias, D. C.; Novoselov, K. S.; Ponomarenko, L. A.; Geim, A. K.; Gorbachev, R. Cross-Sectional Imaging of Individual Layers and Buried Interfaces of Graphene-Based Heterostructures and Superlattices. *Nat. Mater.* **2012**, *11*, 764–767.
20. Riedl, C.; Coletti, C.; Iwasaki, T.; Zakharov, A. A.; Starke, U. Quasi-Free-Standing Epitaxial Graphene on SiC Obtained by Hydrogen Intercalation. *Phys. Rev. Lett.* **2009**, *103*, 246804.
21. Lin, Y.-C.; Lu, C.-C.; Yeh, C.-H.; Jin, C.; Suenaga, K.; Chiu, P.-W. Graphene Annealing: How Clean Can It Be? *Nano Lett.* **2012**, *12*, 414–419.
22. Robinson, J. A.; Hollander, M.; LaBella, M., III; Trumbull, K. A.; Cavalero, R.; Snyder, D. W. Epitaxial Graphene Transistors: Enhancing Performance *via* Hydrogen Intercalation. *Nano Lett.* **2011**, *11*, 3875–3880.
23. Wilson, J. A.; Yoffe, A. D. The Transition Metal Dichalcogenides Discussion and Interpretation of the Observed Optical, Electrical and Structural Properties. *Adv. Phys.* **1969**, *18*, 193–335.
24. Koma, A. van der Waals Epitaxy—A New Epitaxial Growth Method for a Highly Lattice-Mismatched System. *Thin Solid Films* **1992**, *216*, 72–76.
25. Skylaris, C.-K.; Haynes, P. D.; Mostofi, A. A.; Payne, M. C. Introducing ONETEP: Linear-Scaling Density Functional Simulations on Parallel Computers. *J. Chem. Phys.* **2005**, *122*, 084119.
26. Perdew, J. P.; Zunger, A. Self-Interaction Correction to Density-Functional Approximations for Many-Electron Systems. *Phys. Rev. B* **1981**, *23*, 5048–5079.
27. Roehrl, J.; Hundhausen, M.; Emtsev, K. V.; Seyller, Th.; Graupner, R.; Ley, L. Raman Spectra of Epitaxial Graphene on SiC (0001). *Appl. Phys. Lett.* **2008**, *92*, 201918–201920.
28. a) Lee, Y.-H.; Zhang, X. Q.; Zhang, W.; Chang, M.-T.; Lin, C.-T.; Chang, K.-D.; Yu, Y.-C.; Wang, J. T.-W.; Chang, C.-S.; Li, L.-J.; *et al.* Synthesis of Large-Area MoS_2 Atomic Layers with Chemical Vapor Deposition. *Adv. Mater.* **2012**, *24*, 2320–2325. b) Najmaei, S.; Liu, Z.; Zhou, W.; Zou, X.; Shi, G.; Lei, S.; Yakobson, B. I.; Idrobo, J.-C.; Ajayan, P. M.; Lou, J. Vapour Phase Growth and Grain Boundary Structure of Molybdenum Disulphide Atomic Layers. *Nat. Mater.* **2012**, *8*, 754–759.
29. Choi, J. S.; Kim, J. S.; Byun, I. S.; Lee, D. H.; Lee, M. J.; Park, B. H.; Lee, C.; Yoon, D.; Cheong, H.; Lee, K. H.; *et al.* Friction Anisotropy−Driven Domain Imaging on Exfoliated Monolayer Graphene. *Science* **2011**, *333*, 607–610.
30. Robinson, J. A.; Puls, C. P.; Staley, N. E.; Stitt, J. P.; Fanton, M. A.; Emtsev, K. V.; Seyller, T.; Liu, Y. Raman Topography and Strain Uniformity of Large-Area Epitaxial Graphene. *Nano Lett.* **2009**, *9*, 964–968.
31. Bissett, M. A.; Konabe, S.; Okada, S.; Masaharu Tsuji, M.; Ago, H. Enhanced Chemical Reactivity of Graphene Induced by Mechanical Strain. *ACS Nano* **2013**, *7*, 10335–10343.
32. Lee, C.; Yan, H.; Brus, L. E.; Heinz, T. F.; Hone, J.; Ryu, S. Anomalous Lattice Vibrations of Single- and Few-Layer MoS_2. *ACS Nano* **2010**, *4*, 2695–2700.
33. Gong, C.; Huang, C.; Miller, J.; Cheng, L.; Hao, Y.; Cobden, D.; Kim, J.; Ruoff, R. S.; Wallace, R. M.; Cho, K.; *et al.* Metal Contacts on Physical Vapor Deposited Monolayer MoS_2. *ACS Nano* **2013**, *7*, 11350–11357.
34. Liu, K.-K.; Zhang, W.; Lee, Y.-H.; Lin, Y.-C.; Chang, M.-T.; Su, C.-Y.; Chang, C.-S.; Li, H.; Shi, Y.; Zhang, H.; *et al.* Growth of Large-Area and Highly Crystalline MoS_2 Thin Layers on Insulating Substrates. *Nano Lett.* **2012**, *12*, 1538–1544.
35. Baskaran, A.; Smereka, P. Mechanisms of Stranski-Krastanov Growth. *J. Appl. Phys.* **2012**, *111*, 044321–044321.
36. Tang, S.; Ding, G.; Xie, X.; Chen, J.; Wang, C.; Ding, X.; Huang, F.; Lu, W.; Jiang, M. Nucleation and Growth of Single Crystal Graphene on Hexagonal Boron Nitride. *Carbon* **2012**, *50*, 329–331.
37. Kim, K. K.; Reina, A.; Shi, Y.; Park, H.; Li, L.-J.; Lee, Y. H.; Kong, J. Enhancing the Conductivity of Transparent Graphene Films *via* Doping. *Nanotechnology* **2010**, *21*, 285205.
38. Li, Q.; Newberg, J. T.; Walter, E. C.; Hemminger, J. C.; Penner, R. M. Polycrystalline Molybdenum Disulfide (2H-MoS_2) Nano- and Microribbons by Electrochemical/Chemical Synthesis. *Nano Lett.* **2004**, *4*, 277–281.
39. Yin, Z.; Li, H.; Li, H.; Jiang, L.; Shi, Y.; Sun, Y.; Lu, G.; Zhang, Q.; Chen, X.; Zhang, H. Single-Layer MoS_2 Phototransistors. *ACS Nano* **2012**, *6*, 74–80.
40. Zhang, W.; Chuu, C.-P.; Huang, J.-K.; Chen, C.-H.; Tsai, M.-L.; Chang, Y.-H.; Liang, C.-T.; Chen, Y.-Z.; Chueh, Y.-L.; He, J.-H.; *et al.* Ultrahigh-Gain Phototransistors Based on Atomically Thin Graphene-MoS_2 Heterostructures. *Sci. Rep.* **2014**, *4*, 3826.
41. Robinson, J. A.; LaBella, M.; Zhu, M.; Hollander, M.; Kasarda, R.; Hughes, Z.; Trumbull, K.; Cavalero, R.; Snyder, D. Contacting Graphene. *Appl. Phys. Lett.* **2011**, *98*, 053103–053105.
42. Popov, I.; Seifert, G.; Tomanek, D. Designing Electrical Contacts to MoS_2 Monolayers: A Computational Study. *Phys. Rev. Lett.* **2012**, *108*, 156802.
43. Das, S.; Appenzeller, J. Screening and Interlayer Coupling in Multilayer MoS_2. *Phys. Status Solidi RRL* **2013**, *7*, 168–273.
44. Perea-López, N.; Elías, A. L.; Berkdemir, A.; Castro-Beltran, A.; Gutiérrez, H. R.; Feng, S.; Lv, R.; Hayashi, T.; López-Urías, F.; Ghosh, S.; *et al.* Photosensor Device Based on Few-Layered WS_2 Films. *Adv. Funct. Mater.* **2013**, *23*, 5511–5517.
45. Bernardi, M.; Palummo, M.; Grossman, J. C. Extraordinary Sunlight Absorption and One Nanometer Thick Photovoltaics Using Two-Dimensional Monolayer Materials. *Nano Lett.* **2013**, *13*, 3664–3670.
46. Trehan, R.; Lifshitz, Y.; Rabalais, J. W. Auger and X-ray Electron Spectroscopy Studies of hBN, cBN, and N^+_2 Ion Irradiation of Boron and Boron Nitride. *J. Vac. Sci. Technol., A* **1990**, *8*, 4026–4032.
47. Moulder, J. F.; Stickle, W. F.; Sobol, P. E.; Bombem, D. In *Handbook of X-ray Photoelectron Spectroscopy*; Chastain, J., Ed.; Perkin Elmer Co.; Eden Prairie, MN, 1992.